



Scaling CO₂–brine mixing in permeable media via analogue models

J.A. Letelier^{1,†}, H.N. Ulloa^{2,†}, J. Leyrer¹ and J.H. Ortega³

¹Departamento de Ingeniería Civil, Universidad de Chile, Avenida Blanco Encalada 2002, Santiago de Chile

²Department of Earth and Environmental Science, University of Pennsylvania, PA, USA

³Departamento de Ingeniería Matemática y Centro de Modelamiento Matemático, IRL 2807 CNRS-UChile, Universidad de Chile, Avenida Beauchef 851, Santiago de Chile

(Received 23 July 2022; revised 17 March 2023; accepted 19 March 2023)

Supercritical CO₂ injection and dissolution into deep brine aquifers allow its sequestration within geological formations. After injection, CO₂ gas phase is buoyancy-driven over the denser aqueous brine, reaching an apparent gravitational stable distribution. However, CO₂ dissolution in brine propels convection since the mixture is even denser than the underlying brine. This process still needs to be characterised comprehensively. Here, we investigate the irreversible mixing of dissolved CO₂ in brine through laboratory-scale numerical experiments utilising the Hele-Shaw model (Letelier *et al.*, *J. Fluid Mech.*, vol. 864, 2019, pp. 746–767) and a fully miscible two-fluid system. In this scenario, mixing the less dense fluid – mimicking CO₂ gas phase – with the heavier fluid – representing aqueous brine – catalyses cabbelling-powered convection. Our numerical simulations recover the laboratory results in porous media by Neufeld *et al.* (*Geophys. Res. Lett.*, vol. 37, issue 22, 2010, L22404) and may explain the scaling law obtained by Backhaus *et al.* (*Phys. Rev. Lett.*, vol. 106, issue 10, 2011, 104501) in Hele-Shaw cells. More remarkably, we show that the mass flux between the two analogue fluids, characterised by the Sherwood number Sh , obeys the universal scaling law $Sh \sim Ra \vartheta_{scalar}$, with Ra the Rayleigh number and ϑ_{scalar} the mean scalar dissipation rate. This paper sheds light on the fluid dynamics and solubility trapping in geological carbon sequestration.

Key words: convection in porous media, Hele-Shaw flows

† Email addresses for correspondence: juvenal.letelier@uchile.cl, ulloa@sas.upenn.edu

1. Introduction

Carbon dioxide (CO₂) is the most pervasive greenhouse gas affecting the Earth's climate, and its concentration continues to rise (Arias *et al.* 2021). One of the widely debated geoengineering strategies to decarbonise the atmosphere – and mitigate the impacts of climate change – is geologic carbon sequestration (GCS) within deep brine aquifers (Metz *et al.* 2005; Friedmann 2007). Over the last decade, significant progress has been made in understanding the physics and geochemistry at stake in GCS (Altman *et al.* 2014; Celia *et al.* 2015). It entangles: (i) buoyancy driven flows reaching the uppermost region of deep confined aquifers (stratigraphic trapping); (ii) migration of CO₂ gas phase and weak CO₂ dissolution in brines powering convection in the aqueous phase (solubility trapping); (iii) CO₂ gas phase trapped in the pore space via capillary forces (residual trapping); and (iv) mineral precipitation and fixation of CO₂ into the solid porous matrix (geochemical trapping) (Metz *et al.* 2005; Huppert & Neufeld 2014). However, the complex fluid dynamics of CO₂ in saline aquifers (hydrodynamic trapping) remains challenging and not yet characterised comprehensively. Advancing in characterising and modelling the fluid dynamics is critical to quantify the irreversible mixing of dissolved CO₂ in brine and thus determine the efficacy and constraints of GCS in deep aquifers.

The fundamentals of CO₂ dissolution in brine aquifers have been investigated through analogue models of solutal convection in permeable media, utilising numerical and laboratory experiments (Neufeld *et al.* 2010; Backhaus, Turitsyn & Ecke 2011; Hidalgo *et al.* 2012; Hewitt, Neufeld & Lister 2013; Slim 2014; Amooie, Soltanian & Moortgat 2018). Such experiments have used analogue working fluids within porous media and Hele-Shaw cells to mimic and visualise the convective dynamics associated with the supercritical CO₂ dissolution in brine (Backhaus *et al.* 2011; Hewitt *et al.* 2013; MacMinn & Juanes 2013; Slim *et al.* 2013; Letelier *et al.* 2016; Alipour, De Paoli & Soldati 2020; De Paoli 2021; De Paoli *et al.* 2022). Utilised working fluids and environments include methanol and ethylene-glycol (MEG) mixture with water in a cell filled with sand (Neufeld *et al.* 2010; Guo *et al.* 2021), MEG doped with sodium iodide and sodium chloride in quasi-two-dimensional (Q-2-D) and three-dimensional (3-D) porous media (Wang *et al.* 2016), and an aqueous solution of propylene glycol (PPG) and deionised water in Hele-Shaw cells (Backhaus *et al.* 2011; Hewitt *et al.* 2013).

In the literature, we find two distinctive configurations to investigate solutal convection in porous media: the ‘canonical’ and ‘analogue’ models (Hidalgo *et al.* 2012). In the canonical model, density varies linearly with concentration. In this case, dissolution occurs at the uppermost boundary, whereas a no-flux condition is imposed at the bottom boundary. Conversely, in the analogue model, density varies nonlinearly with concentration. In this case, no-flux conditions are imposed at the top and bottom boundaries. The test fluids used by Neufeld *et al.* (2010), Backhaus *et al.* (2011) and Hewitt *et al.* (2013) satisfy a constitutive equation for density of the type $\rho(S_w) = \rho_B + c_1 S_w + c_2 S_w^2$, with S_w the mass fraction of the less dense fluid component (see table 1 for symbols’ definition). A nonlinear equation for $\rho(S_w)$ enables buoyancy dynamics not supported by linear equations of state, such as ‘cabbelling’, i.e. the formation of an aqueous mixture that is denser than the fluid parcels that gave origin to it (e.g. Groeskamp, Abernathy & Klocker 2016). Cabbelling, in fact, is the mechanism driving convection, downward mass transport and enhancing irreversible mixing between the analogue working fluids. Here, the fundamental quest is the scaling law linking the non-dimensional mass flux, the Sherwood number Sh , the Rayleigh number of the system Ra , and the mean scalar dissipation rate ϑ_{scalar} .

Symbol	Dimensions	Definition	First time used
Sh	—	Sherwood number	§ 1
Ra	—	Rayleigh number	§ 1
ϑ_{scalar}	—	Non-dimensional mean scalar dissipation rate	§ 1
ϵ	—	Anisotropy ratio	§ 2
ρ^*	ML^{-3}	Density of analogue two-fluid system	figure 2.1, § 2
ρ_A	ML^{-3}	Density of the (CO ₂) analogue fluid A	figure 1, § 2
ρ_B	ML^{-3}	Density of the (brine) analogue fluid B	figure 1, § 2
f_ρ^*	ML^{-3}	Dimensional Boussinesq density component	(2.1), § 2
f_ρ	—	Non-dimensional Boussinesq density component	(2.3a–e), § 2
S_w	%	Fluid A mass fraction	§ 1
Δ_w	%	Concentration at which density is maximum	(2.1), § 2
ρ_{max}	ML^{-3}	Maximum density at $S_w = \Delta_w$	(2.2), § 2
b	L	Hele-Shaw cell gap	§ 2
H	L	Hele-Shaw cell height	§ 2
H_{IB}	L	Initial height between fluid A and fluid B	§ 2
L	L	Hele-Shaw cell horizontal length	§ 2
K	L^2	Hele-Shaw cell permeability	§ 2
ν	$L^2 T^{-1}$	Kinematic viscosity	§ 2
κ	$L^2 T^{-1}$	Scalar diffusivity	§ 2
\mathbf{x}^*, \mathbf{x}	L, —	Dimensional and non-dimensional coordinates	(2.3a–e), § 2
t^*, t	T, —	Dimensional and non-dimensional time	(2.3a–e), § 2
\mathbf{v}^*, \mathbf{v}	T, —	Dimensional and non-dimensional velocity field	(2.3a–e), § 2
p^*, p	$ML^{-1} T^{-2}$, —	Dimensional and non-dimensional pressure field	(2.3a–e), § 2

Table 1. Glossary of general symbols used in the text.

In the canonical model, Amooie *et al.* (2018) obtained the sub-linear relationship $Sh \sim Ra^{0.931}$ for 2-D and 3-D numerical simulations solving the non-Boussinesq Darcy equation with no-flux at the lateral boundaries. This result is valid in the range $1500 \lesssim Ra \lesssim 135\,000$. The authors remarked that the linear relation $Sh \sim Ra$ is attained asymptotically (i.e. for $Ra \gtrsim 4 \times 10^4$). The latter has also been reported in other works using non-Boussinesq/Boussinesq fluids and periodic lateral boundaries (Pau *et al.* 2010; Slim 2014). In the case of laboratory experiments (no-flux conditions at the lateral boundaries), the scaling shows a sub-linear trend of the type $Sh \sim Ra^\alpha$. In a Q-2-D porous medium, Guo *et al.* (2021) obtained $\alpha = 0.95$, for $400 \lesssim Ra \lesssim 8000$, while in 3-D porous media, Wang *et al.* (2016) found $\alpha = 0.93$, for $2600 \lesssim Ra \lesssim 16\,000$. These laboratory results show good agreement with numerical results for intermediate Ra . Yet power-law exponents derived from analogue models differ significantly from those obtained from canonical ones. In a Q-2-D porous medium, Neufeld *et al.* (2010) obtained $Sh \sim Ra^{0.84}$, whereas for Hele-Shaw experiments, Backhaus *et al.* (2011) found $Sh \sim Ra^{0.76}$. These results are consistent with the theoretical scaling law $Sh \sim Ra^{4/5}$ derived by Neufeld *et al.* (2010), resulting from a balance between vertical advection and horizontal diffusion. Nonetheless, we stress that the nature of the laboratory-scale environment, i.e. porous media and Hele-Shaw, may impact the scaling law's exponent of Ra . Indeed, we expect that Hele-Shaw cells with larger gaps may lead to smaller exponents (De Paoli, Alipour & Soldati 2020). Additionally, discrepancies between scaling laws $Sh \sim Ra^\alpha$ reported in the

literature may also arise from different boundary conditions set in numerical simulations and laboratory experiments.

In this paper, we investigate the irreversible mixing of dissolved CO₂ in brine through laboratory-scale numerical experiments utilising a fully miscible two-fluid system. Here, we aim to (i) reconcile apparent discrepancies between scaling laws of the type $Sh \sim Ra^\alpha$ employing the Hele-Shaw equations (Letelier, Mujica & Ortega 2019) applied to the analogue model, and (ii) examine the relationship between the non-dimensional mass flux Sh and the irreversible mixing controlled by the mean scalar dissipation rate ϑ_{scalar} . We therefore concentrate on finding relationships of the type $Sh \sim Ra^{\alpha(\epsilon)}$, with ϵ a geometrical scale of the Hele-Shaw cell, to pave the road towards a universal scaling law of the form $Sh/\vartheta_{scalar} = bRa^n$, with b and n independent of ϵ . Such a scaling law may serve for estimating the rate of homogenisation of the dissolved CO₂ in brines.

The paper is organised as follows. In § 2, we introduce the Hele-Shaw model utilised to investigate the problem of cabbeling-powered convection in Q-2-D Hele-Shaw cells as an analogue for the problem of CO₂-brine mixing in permeable media. Then in § 3, we derive global conservation equations for the scalar field representing the CO₂-brine mixture, in order to disentangle the various fluxes involved in the irreversible mixing of the scalar field. The modelling approach is described in § 4, whereas our numerical experiments, benchmarks and scaling results are reported and discussed in § 5. Finally, § 6 summarises our main findings.

2. Hele-Shaw model

We consider a Hele-Shaw domain whose cell gap is b in the y^* coordinate, and whose horizontal length and vertical height are L and H in the x^* and z^* coordinates, respectively. Conceptually, the Hele-Shaw cell fulfils the relation $b \ll H$ and provides a suitable setting to visualise the fluid dynamics in a transparent, Q-2-D porous-like medium of permeability $K = b^2/12$. At the laboratory scale, the cell gaps range from 100 μm to 1 mm, while the cell heights can be of the order of 10 cm. In our model, the cell is filled with an incompressible, density-variable Boussinesq fluid composed of the mixture between two miscible fluids. Both the kinematic viscosity ν and scalar diffusivity κ are assumed to be constant. Figure 1(a) illustrates examples of the density as a function of the water mass fraction (concentration) S_w for aqueous solutions of PPG used to model the CO₂-brine mixture in laboratory experiments. The density of the fluid mixture is modelled by the nonlinear constitutive relationship

$$\rho^*(S_w) = \rho_B + f_\rho^*(S_w) = \rho_B + (\rho_B - \rho_A) \left[\left(\frac{2\Delta_w}{1 - 2\Delta_w} \right) S_w - \left(\frac{1}{1 - 2\Delta_w} \right) S_w^2 \right], \quad (2.1)$$

with $f_\rho^* = \rho^* - \rho_B$ the Boussinesq density component, ρ_A and ρ_B reference densities shown in figure 1(b), and Δ_w the concentration at which the fluid density is maximum,

$$\rho^*(\Delta_w) = \rho_{max} = \rho_B + \Delta_w^2 \left(\frac{\rho_B - \rho_A}{1 - 2\Delta_w} \right). \quad (2.2)$$

Figure 1(b) schematises the boundary and initial conditions of our problem. Initially, the fluid A of uniform density ρ_A is placed over the fluid B of uniform density ρ_B . The initial interface between fluid A and fluid B is located at height $H_{IB} < H$. Tracking this interface (and its height) is relevant since that is where molecular mixing between both fluids and cabbeling occur.

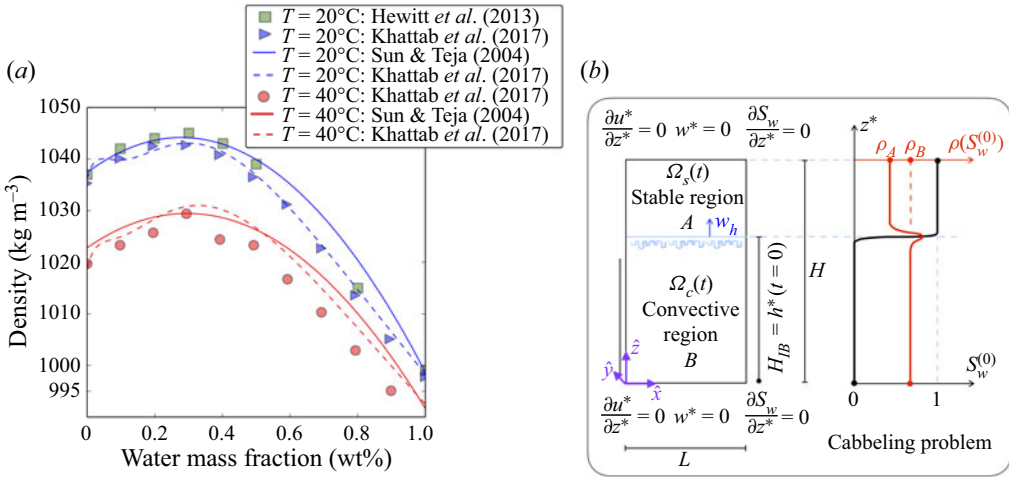


Figure 1. (a) Density of the aqueous solution of PPG as a function of the water mass fraction (concentration) S_w and temperature. For a fixed temperature, density satisfies approximately the constitutive relation $\rho(S_w) = \rho_B + c_1 S_w + c_2 S_w^2$ (Sun & Teja 2004; Hewitt et al. 2012; Khattab et al. 2017); see (2.1). The parameters c_1 and c_2 are constants, and ρ_B is the density of the fluid mimicking the brine layer. (b) Conceptual model for the analogue fluid problem in a Hele-Shaw cell, mimicking the CO₂-brine mixing. The cell gap b is much thinner than the cell height H , so the 3-D system can be approximated as a Q-2-D geometry, with u^* the velocity component in the lateral (horizontal) direction (\hat{x}), and w^* the velocity component in the vertical direction (\hat{z}). We impose no-flux ($\partial S_w / \partial z^* = 0$) and free-slip ($w^* = 0, \partial u^* / \partial z = 0$) boundary conditions, at both $z^* = 0$ and $z^* = H$. Initially, a layer of fluid A of density ρ_A , mimicking the CO₂ gas phase, lays over a layer of fluid B of density $\rho_B > \rho_A$ that mimics an aqueous brine layer. Both fluids are fully miscible. The initial concentration $S_w^{(0)}(z^*)$ and density $\rho(S_w^{(0)})$ profiles are shown in black and red, respectively. Molecular diffusion between A and B leads to cabbeling, which catalyses the growth of finger-like instabilities and active convection in the region B.

We consider the following non-dimensional forms of the dimensional variables $\mathbf{x}^*, t^*, \mathbf{v}^*, p^*, f_\rho^*$:

$$\mathbf{x} = \frac{\mathbf{x}^*}{H_{IB}}, \quad t = \frac{t^*}{H_{IB}/u_c}, \quad \mathbf{v} = \frac{\mathbf{v}^*}{u_c}, \quad p = \frac{\tilde{p}^*}{p_c} \quad \text{and} \quad f_\rho = \frac{f_\rho^*}{\Delta \rho_m} = 2 \frac{S_w}{\Delta_w} - \frac{S_w^2}{\Delta_w^2}, \quad (2.3a-e)$$

with $\Delta \rho_m = \rho_{max} - \rho_B$ the maximum density difference respect to the deeper fluid B, $\mathbf{x} = x \hat{x} + z \hat{z}$ the non-dimensional position, velocity $\mathbf{v} = u \hat{x} + w \hat{z}$ the non-dimensional velocity, $u_c = \Delta \rho_m g K / (\rho_B \nu)$ the characteristic velocity, and $p_c = \rho_B \nu u_c H_{IB} / K$ the characteristic pressure. Considering the above geometrical and fluid properties, the non-dimensional 2-D Hele-Shaw equations (Letelier et al. 2019) are

$$\partial_i v_i = 0, \quad (2.4a)$$

$$\epsilon^2 \frac{Ra}{Sc} \left(\frac{6}{5} \frac{\partial v_i}{\partial t} + \frac{54}{35} v_j \partial_j v_i \right) = -\partial_i p - f_\rho(S_w) \delta_{iz} - v_i + \epsilon^2 \partial_j^2 v_i + \frac{2}{35} \epsilon^2 Ra (v_j \partial_j S_w) \frac{df_\rho}{dS_w} \delta_{iz}, \quad (2.4b)$$

$$\frac{\partial S_w}{\partial t} + v_i \partial_i S_w = \frac{1}{Ra} \partial_i^2 S_w + \frac{2}{35} \epsilon^2 Ra \partial_j ((v_i \partial_i S_w) v_j), \quad (2.4c)$$

with $df_\rho/dS_w = (2/\Delta_w)(1 - S_w/\Delta_w)$ the derivative of the Boussinesq density, whereas

$$\epsilon = \frac{\sqrt{K}}{H_{IB}}, \quad Ra = \frac{u_c H_{IB}}{\kappa} = \frac{\Delta \rho_m g K H_{IB}}{\rho_B \nu \kappa} \quad \text{and} \quad Sc = \frac{\nu}{\kappa} \quad (2.5a-c)$$

are the anisotropy ratio, the Rayleigh number for Hele-Shaw cells and the Schmidt number, respectively. The Hele-Shaw equations (2.4) are valid for $\epsilon \ll 1$, $\epsilon^2 Ra \ll 1$ and $Sc \geq 1$, and they result from averaging the Navier–Stokes equation in the spanwise \hat{y} direction. This averaging procedure of the velocity, pressure and concentration fields in \hat{y} integrates no-slip and no-flux boundary conditions at the vertical walls (Letelier *et al.* 2019). Free-slip and no-flux are imposed on the top and bottom boundaries, as shown in figure 1(b). We consider two scenarios for the lateral boundaries, no-flux and free-slip conditions (closed system), and periodic boundary conditions. For $\epsilon \rightarrow 0$, the model (2.4) reduces to the Darcy equation coupled with the advection–diffusion model (e.g. Hewitt, Neufeld & Lister 2012). Notice that in nature, the Schmidt number of CO₂–brine mixtures is about 10³, while for analogue fluids utilised in laboratory experiments, $10 \leq Sc \leq 100$. Moreover, regardless of the flow regime (Darcian or Hele-Shaw), we note that greater Schmidt numbers will weaken the inertial effects in the momentum balance (2.4b), making mechanical dispersion the most relevant term affecting convective dynamics beyond the Darcian regime (Liang *et al.* 2018).

3. Global conservation equations

We study global quantities associated with mass transfer and mixing in the time-dependent domain $\Omega_c(t)$ sketched in figure 1(b). The (dimensional) averaged height $h^*(t)$ defines the upper boundary of Ω_c , with $h^*(t = 0) = H_{IB}$. For $t > 0$, the definition and computation of h^* are somewhat arbitrary and depend on authors’ criteria. Nevertheless, the global conservation equations introduced in this section are independent of the chosen criteria; our definition of h^* and method adopted to compute it are introduced in § 3.1.

Henceforth, we express the ‘mean’ of a physical variable $f(t, \mathbf{x})$ through the lateral (\hat{x} direction) and domain integrals as

$$\langle f \rangle_\ell(t, z) = \frac{1}{\mathcal{L}} \int_0^{\mathcal{L}} f(t, \mathbf{x}) dx \quad \text{and} \quad \langle f \rangle_\nu(t) = \int_0^{h(t)} \langle f \rangle_\ell(t, z) dz, \quad (3.1a,b)$$

respectively, with $\mathcal{L} = L/H_{IB}$ the effective cell aspect ratio, and $h(t) = h^*(t)/H_{IB}$ the non-dimensional averaged height. Likewise, we express the time average of a function $f(t)$ over a window of size τ as

$$\langle f \rangle_\tau = \frac{1}{\tau} \int_t^{t+\tau} f(\tilde{t}) d\tilde{t}. \quad (3.2)$$

3.1. Interface detection and first conservation equation

For an arbitrary 2-D ‘control volume’ $\Omega(t)$, the Reynolds transport theorem establishes that the rate of change of a non-dimensional quantity $\int_{\Omega(t)} f(t, x, z) dx dz$ is given by

$$\frac{d}{dt} \left[\int_{\Omega(t)} f dx dz \right] = \int_{\Omega(t)} \frac{\partial f}{\partial t} dx dz + \oint_{\partial\Omega(t)} f v_i n_i ds, \quad (3.3)$$

with $\partial\Omega$ the boundary of the ‘volume’ Ω , ds the infinitesimal ‘length’ of $\partial\Omega$, and v_i the i th component of the (non-dimensional) velocity at $\partial\Omega$. Let us now consider $f = S_w$.

Applying (3.3) over a specific volume Ω_c and normalising by \mathcal{L} , we obtain

$$\frac{1}{\mathcal{L}} \int_{\Omega_c(t)} \frac{\partial S_w}{\partial t} dx dz = \frac{1}{\mathcal{L}} \frac{d}{dt} \left[\int_{\Omega_c(t)} S_w dx dz \right] - \frac{1}{\mathcal{L}} \int_0^{\mathcal{L}} w_h S_w \Big|_{z=h} dx, \quad (3.4)$$

where w_h corresponds to the rate of change over time of $h(t)$. Using (3.1a,b) and assuming that w_h is a constant (Neufeld *et al.* 2010), (3.4) can be written compactly as

$$\left\langle \frac{\partial S_w}{\partial t} \right\rangle_v = \frac{d}{dt} \langle S_w \rangle_v - w_h \langle S_w \rangle_\ell \Big|_{z=h}, \quad (3.5)$$

with $\langle S_w \rangle_\ell|_{z=h}$ the horizontal average of S_w evaluated at $h(t)$. Thus the transport equation governing the water mass fraction over the domain Ω_c is obtained by integrating (2.4c), i.e.

$$\int_{\Omega_c} \frac{\partial S_w}{\partial t} dx dz + \int_0^{\mathcal{L}} \left[S_w - \frac{2}{35} \epsilon^2 Ra (v_i \partial_i S_w) \right] w \Big|_{z=h} dx = \frac{1}{Ra} \int_0^{\mathcal{L}} \frac{\partial S_w}{\partial z} \Big|_{z=h} dx. \quad (3.6)$$

Using (3.5) and the mean quantities defined in (3.1a,b), (3.6) can be contracted to

$$Ra \frac{d}{dt} \langle S_w \rangle_v = -\mathcal{F}_{ad} + Ra w_h \langle S_w \rangle_\ell|_{z=h} + \frac{\partial \langle S_w \rangle_\ell}{\partial z} \Big|_{z=h}, \quad (3.7)$$

with \mathcal{F}_{ad} the advective–dispersive flux defined as

$$\mathcal{F}_{ad} = Ra \langle S_w w \rangle_\ell|_{z=h} - \frac{2}{35} \epsilon^2 Ra^2 \langle w \partial_i (S_w v_i) \rangle_\ell|_{z=h}. \quad (3.8)$$

Previous authors have chosen different criteria to define and compute $h(t)$. Neufeld *et al.* (2010) studied the laterally averaged concentration profile and used the ‘flat’ interfacial region – which propagated upwards at a constant speed – to estimate an advective mass flux. In contrast, Hewitt *et al.* (2013) defined h as the averaged interfacial height where $\langle S_w \rangle_\ell|_{z=h} = \Delta_w$, i.e. the position at which the horizontally averaged density is maximum. The ‘interface’, with height $h_{int}(t, x)$, is defined as the contour satisfying $S_w(x, z = h_{int}(t, x)) = \Delta_w$. This locus is geometrically complex and not flat (see figure 2b) (e.g. Hidalgo *et al.* 2015). Another alternative is to define h as the solution of the equation $\mathcal{F}_{ad} = 0$ in (3.8). The latter implies that the mass transfer at $h(t)$ is governed by molecular diffusion $\partial_z \langle S_w \rangle_\ell|_{z=h}$ and the flux due to the rejection at constant velocity w_h of the contour drawn by h . The criterion above to determine $h(t)$ is feasible via numerical simulations. However, its application to laboratory experiments is challenging owing to the necessity to resolve the velocity and scalar fields simultaneously.

Here, we define $h(t)$ so that its computation via laboratory or numerical experiments is straightforward. First, we note that $\rho(S_w = 2\Delta_w) = \rho_B$ corresponds to the density of the initial bottom layer (fluid B). Let us introduce $h_{iso}(t, x)$ as the contour satisfying $S_w(x, h_{iso}(t, x)) = 2\Delta_w$. This locus is substantially flatter (quasi-flat) than the case of the ‘interface’ $h_{int}(t, x)$ (compare figures 2b,c). The latter allows us to define the averaged height $h(t)$ robustly as the solution of $\langle S_w \rangle_\ell|_{z=h} = 2\Delta_w$. This h splits the Hele-Shaw cell into two time-dependent rectangular domains, a convective region $\Omega_c(t)$, and a stable region $\Omega_s(t)$, as in figure 1(b).

A global description of the problem requires studying the convective dynamics of the ‘free-falling’ plumes, i.e. from the state in which the downward plumes are sufficiently

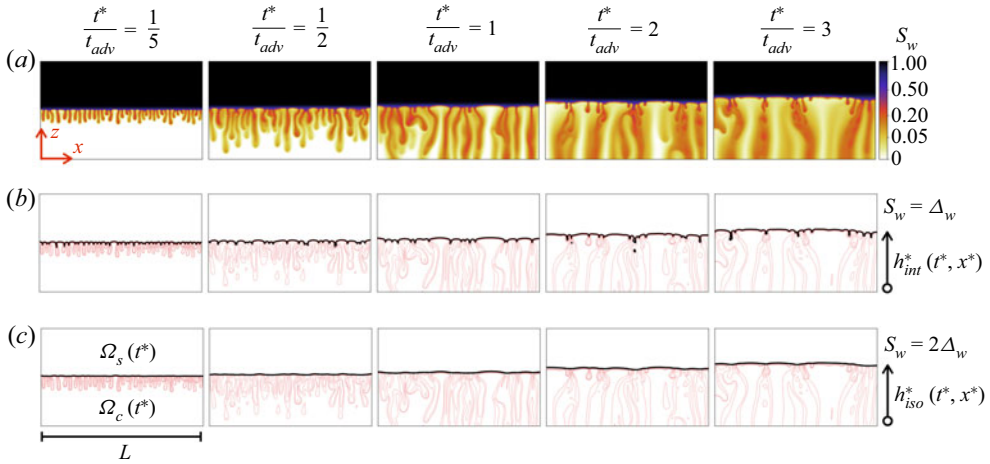


Figure 2. (a) Spatiotemporal evolution of the scalar field S_w modelling the mixing of the initial two-fluid system in a Hele-Shaw cell mimicking the CO_2 -brine mixture. The plotted area highlights the transition between the upper stable layer and the deeper convective layer. (b) Spatiotemporal evolution of the isoscalar $S_w = \Delta_w$ drawn with the dimensional height (‘interface’) $h_{int}^*(t^*, x^*)$, defining the locus of the maximum density (Hewitt *et al.* 2013). This locus is not flat. (c) Spatiotemporal evolution of the isoscalar $S_w = 2\Delta_w$ drawn by the height $h_{iso}^*(t^*, x^*)$, found above the ‘interface’. This locus is substantially flatter in comparison to (b), allowing us to define a robust averaged height $h(t)$ (in its non-dimensional form).

spaced from local mergers beneath the interface until the first megaplume reaches the bottom of the Hele-Shaw cell. This regime is known as the constant flux (Slim 2014) or late convection (Amooie *et al.* 2018). The time window τ that captures the stage of free-falling convective plumes is denoted as the integral time scale. Over this time scale, physical quantities such as $d\langle S_w \rangle_v / dt$, dh/dt and $\partial \langle S_w \rangle_\ell / \partial z|_{z=h}$ have a statistically stationary behaviour (see § 5). Therefore, applying the time average defined in (3.2) and the ‘normalised’ scalar field $\varphi = S_w / 2\Delta_w$, (3.7) can be written as

$$\left\langle Ra \frac{d}{dt} \langle \varphi \rangle_v \right\rangle_\tau = -\frac{1}{2\Delta_w} \langle \mathcal{F}_{ad} \rangle_\tau + Ra w_h + \left\langle \frac{\partial \langle \varphi \rangle_\ell}{\partial z} \Big|_{z=h} \right\rangle_\tau. \quad (3.9)$$

Equation (3.9) denotes the first conservation law utilised to characterise the mass transfer rate between the fluid A (CO_2 gas phase) and fluid B (aqueous brine layer). Within the integral time scale, $O(\mathcal{F}_{ad} / (2\Delta_w)) \ll O(Ra w_h)$, $\langle \partial \langle \varphi \rangle_\ell / \partial z|_{z=h} \rangle_\tau$, i.e. the contribution of \mathcal{F}_{ad} can be ignored. The latter is shown in the Appendix, figure 10. Interestingly, each of the remainder terms in (3.9) can be interpreted as a non-dimensional parameter. The time average of the mean scalar rate of change is defined as the ‘global’ Sherwood number

$$Sh_\varphi = \left\langle Ra \frac{d}{dt} \langle \varphi \rangle_v \right\rangle_\tau. \quad (3.10)$$

De Paoli *et al.* (2020) used a similar version of (3.10) to construct the scaling law associated with the dissolution rate of potassium permanganate, KMnO_4 , into water in a Hele-Shaw cell, whereas Guo *et al.* (2021) adopted (3.10) to estimate the dissolution rate of MEG in pure H_2O within a porous medium. On the other hand, the ‘local’ Sherwood

number, defined as

$$Sh = Ra w_h, \tag{3.11}$$

is based on the rate at which the contour $h_{iso}(t, x)$ expands vertically in response to the mass exchange. Neufeld *et al.* (2010) used a similar version of Sh to construct the scaling law associated with the dissolution of MEG into H₂O in a porous medium. In addition, the term $\langle \partial \langle \varphi \rangle_v / \partial z |_{z=h} \rangle_\tau$ in (3.9) can be interpreted as a solutal Nusselt number,

$$Nu_\varphi = \left\langle \frac{\partial \langle \varphi \rangle_\ell}{\partial z} \Big|_{z=h} \right\rangle_\tau, \tag{3.12}$$

which is analogous to the Nusselt number employed to quantify the global heat transfer rate due to thermal convection in porous media (Hewitt *et al.* 2012) and Hele-Shaw cells (Letelier *et al.* 2019).

If the control volume Ω_c is extended over the whole domain (see figure 1b), then the conservation equation for $\langle \varphi \rangle$ simplifies to

$$\frac{d}{dt} \langle \varphi \rangle = 0, \quad \text{with} \langle \varphi \rangle = \frac{1}{\mathcal{L}} \int_0^{\mathcal{H}} \int_0^{\mathcal{L}} \varphi(t, x, z) dx dz, \tag{3.13}$$

where $\mathcal{H} = H/H_{IB}$. The mass budget in (3.13) shows the relevance of using a time-dependent control volume $\Omega_c(t)$ to disentangle the physics and quantify the mass transfer between the quiescent upper layer and the deeper convective mixing layer.

3.2. Second conservation equation

We investigate the irreversible mixing in the system through the evolution of the scalar variance φ^2 . The equation governing the rate of change of φ^2 can be derived by multiplying (2.4c) by S_w . Averaging the resulting equation over the domain Ω_c and relocating Ra , the evolution equation for $\langle \varphi^2/2 \rangle_v$ is given by

$$Ra \frac{d}{dt} \left\langle \frac{1}{2} \varphi^2 \right\rangle_v = -\mathcal{F}_{var} + Ra w_h \left\langle \frac{1}{2} \varphi^2 \right\rangle_\ell \Big|_{z=h} + \frac{\partial}{\partial z} \left\langle \frac{1}{2} \varphi^2 \right\rangle_\ell \Big|_{z=h} - Ra \langle \Phi_{scalar}^{(\epsilon)} \rangle_v, \tag{3.14}$$

with \mathcal{F}_{var} the variance flux, and $\Phi_{scalar}^{(\epsilon)}$ the scalar dissipation rate, defined as

$$\mathcal{F}_{var} = Ra \left\langle \frac{1}{2} \varphi^2 w \right\rangle_\ell \Big|_{z=h} - \frac{2}{35} \epsilon^2 Ra^2 \left\langle w \partial_i \left(\frac{1}{2} \varphi^2 v_i \right) \right\rangle_\ell \Big|_{z=h}, \tag{3.15}$$

$$\Phi_{scalar}^{(\epsilon)} = \frac{1}{Ra} (\partial_i \varphi)^2 + \frac{2}{35} \epsilon^2 Ra (\partial_i (\varphi v_i))^2. \tag{3.16}$$

The physics of $\langle \Phi_{scalar}^{(\epsilon)} \rangle_v$ can be interpreted straightforwardly by extending the control volume to the entire Hele-Shaw cell. Applying the domain average defined in (3.13) and the adiabatic boundary conditions for the Hele-Shaw cell, (3.14) reduces to

$$Ra \frac{d}{dt} \left\langle \frac{1}{2} \varphi^2 \right\rangle = -Ra \langle \Phi_{scalar}^{(\epsilon)} \rangle. \tag{3.17}$$

The right-hand side term in (3.17) is a negative-definite quantity that determines the global decay rate of the scalar variance (Ulloa & Letelier 2022). As a result, $\langle \frac{1}{2} \varphi^2 \rangle(t)$ is a monotonically decreasing function in time owing to irreversible mixing and

homogenisation of the scalar φ (i.e. S_w) inside the fluid environment. If the rate of change of the mean scalar variance $\langle \varphi^2/2 \rangle_v$ is statistically constant over the integral time scale τ , then we can characterise the quasi-steady fluxes governing the scalar variance transport and irreversible mixing in Ω_c as

$$Ra \left\langle \frac{d}{dt} \left\langle \frac{1}{2} \varphi^2 \right\rangle_v \right\rangle_\tau = -\langle \mathcal{F}_{var} \rangle_\tau + Ra \left\langle w_h \left\langle \frac{1}{2} \varphi^2 \right\rangle_\ell \Big|_{z=h} \right\rangle_\tau + \left\langle \frac{\partial}{\partial z} \left\langle \frac{1}{2} \varphi^2 \right\rangle_\ell \Big|_{z=h} \right\rangle_\tau - Ra \vartheta_{scalar}, \tag{3.18}$$

with $\vartheta_{scalar} = \langle \langle \Phi_{scalar}^{(\epsilon)} \rangle_v \rangle_\tau$ the mean scalar dissipation rate. Equation (3.18) corresponds to the second conservation law of the fluid environment investigated here.

4. Method: numerical experiments

We performed numerical experiments using the spectral solver `flow_solve` (Winters 2012), which has been applied successfully to resolve buoyancy-driven flows in Hele-Shaw cells (Letelier *et al.* 2019; Ulloa & Letelier 2022). The dynamical variables in (2.4a)–(2.4c) were expanded by means of trigonometric basis functions over the Hele-Shaw computational domain, and integrated in time using a third-order Adams–Bashforth scheme for advective/buoyant terms and the implicit fourth-order Adams–Moulton method for diffusive scheme.

The problem of irreversible mixing between dissolved CO₂ and brine does not admit a base state solution. The initial condition for the scalar field is given by

$$S_w^{(0)}(z) = 1 - \frac{H_{IB}}{H} - \frac{2}{\pi} \sum_{n=1}^N \frac{1}{n} \sin\left(\frac{n\pi H_{IB}}{H}\right) \cos\left(\frac{n\pi z}{H}\right) \exp(-n^2 \pi^2 \bar{t}), \quad \bar{t} \ll 1, \tag{4.1}$$

whereas the velocity components satisfy $(u, w)|_{t=0} = (0, 0)$. To fulfil the boundary conditions defined in figure 1(b), we expanded $u \sim f_u(n_x, x) \cos(n_z \pi z)$, $w \sim f_w(n_x, x) \sin(n_z \pi z)$, $p \sim f_p(n_x, x) \cos(n_z \pi z)$ and $S_w \sim f_s(n_x, x) \cos(n_z \pi z)$, with n_x and n_z the number of grid points in x and z coordinates, respectively. The functions f_β , with $\beta \in \{u, w, p, s\}$, depend on lateral boundary conditions. For no-flux, free-slip lateral conditions, $f_u = \sin(n_x \pi x)$ and $f_w = f_p = f_s = \cos(n_x \pi x)$. On the other hand, for periodic lateral conditions, $f_u = f_w = f_p = f_s = \exp(n_x \pi x)$. The effective cell aspect ratio was $\mathcal{L} = L/H_{IB} = 2/3$, while the entire domain aspect ratio was $L/H = 1/2$.

For no-flux, free-slip lateral conditions, the dimensional spatial resolutions in x and z were $\Delta_x^* = L/(n_x - 1)$ and $\Delta_z^* = H/(n_z - 1)$, respectively, such that $\Delta = \Delta_x^* = \Delta_z^*$. Likewise, for periodic lateral conditions, we keep the homogeneity of the grid Δ , but $\Delta_x^* = L/n_x$ because the point $x(n_x)$ is not stored explicitly in `flow_solve`. The resolution Δ was chosen to resolve the spectral Batchelor scale $\Delta \leq \pi \Delta_b$ (Grötzbach 1983), with $\Delta_b = (\nu^3/\varepsilon Sc^2)^{1/4}$ the Batchelor length scale, and $\varepsilon \sim \nu u_c^2/K$ the scale of the kinetic energy dissipation rate. The time step met the Courant–Friedrichs–Lewy (CFL) condition of the numerical scheme, $CFL \leq 0.02$, for both velocity components (Letelier *et al.* 2019).

The horizontal average of a function $f_i = f(x_i)$ over n_x grid points was based on a cubic spline interpolation of f in a three times denser grid, with $m_x = 3n_x$ points. The interpolated function f_j^{new} , with $j = 1, \dots, m_x$, was integrated using the composite Simpson’s rule. We used the same procedure for the domain average of the

Label	ϵ	Ra	$Pe = \epsilon Ra$	$n_x \times n_z$	Sh_ϕ	$Sh_\phi^{(m)}$
A1	5×10^{-4}	1200	0.6	403×805	37.79	1.89×10^{-2}
A2	5×10^{-4}	3600	1.8	573×1145	103.84	5.12×10^{-2}
A3	5×10^{-4}	6000	3.0	669×1337	160.00	8.00×10^{-2}
A4	5×10^{-4}	8400	4.2	803×1605	205.16	10.26×10^{-2}
A5	5×10^{-4}	12 000	6.0	1003×2005	295.50	14.78×10^{-2}
A6	5×10^{-4}	36 000	18.0	1673×3345	707.41	35.37×10^{-2}
B1	3×10^{-3}	7200	21.6	495×991	143.84	4.32×10^{-1}
B2	3×10^{-3}	14 400	43.2	661×1321	212.12	6.36×10^{-1}
B3	3×10^{-3}	21 600	64.8	825×1651	262.87	7.89×10^{-1}
B4	3×10^{-3}	28 800	86.4	925×1849	317.59	9.53×10^{-1}
C1	5×10^{-3}	600	3.0	71×141	18.36	9.18×10^{-2}
C2	5×10^{-3}	1200	6.0	101×201	34.41	17.21×10^{-2}
C3	5×10^{-3}	3600	18.0	173×345	86.68	43.34×10^{-2}
C4	5×10^{-3}	6000	30.0	213×425	121.51	60.76×10^{-2}
C5	5×10^{-3}	8400	42.0	257×513	147.97	73.99×10^{-2}
C6	5×10^{-3}	12 000	60.0	337×673	172.35	86.18×10^{-2}
C7	5×10^{-3}	24 000	120.0	427×853	241.29	120.65×10^{-2}

Table 2. Summary of non-dimensional experimental parameters and results. The experimental set is conformed by three subsets, each of them characterised by single anisotropy ratio ϵ and a range of Rayleigh Ra and Péclet $Pe = \epsilon Ra$ numbers. The Schmidt number $Sc = 10$ was kept constant for all our experiments. Here, Sh_ϕ is the Sherwood number introduced in (3.11), and $Sh_\phi^{(m)} = \epsilon Sh_\phi$ is the modified Sherwood number computed from the numerical results.

z -dependent function. Numerical derivatives were computed using a spectral approach based on sine and cosine transforms, depending on the boundary conditions.

Our numerical experiments encompassed $10^3 \leq Ra \leq 3 \times 10^4$, with $Sc = 10$, and three values of the anisotropy ratio, $\epsilon = 5 \times 10^{-4}$, $\epsilon = 3 \times 10^{-3}$ and $\epsilon = 5 \times 10^{-3}$. The simulations were run in high-performance computers using up to 80 cores over four advective time scales, defined as $H_{IB}^2/(\kappa Ra)$. This simulation time was enough to resolve the full transition from the onset of convection to the instant that megaplumes reached the bottom boundary of the Hele-Shaw cell. Table 2 summarises the experimental set and numerical results for the non-dimensional mass flux parameters.

5. Results and discussion

5.1. The adiabatic analogue model in the Darcian regime

In order to have a robust benchmark, we conducted a first set of numerical experiments adopting the laboratory scales employed by Neufeld *et al.* (2010), i.e. an analogue model with no-flux boundary conditions. The cell dimensions used by Neufeld *et al.* (2010) were $b = 1.4$ cm, $L = 40$ cm and $H = 80$ cm, and it was filled with a granular material. The initial position of the interface was $H_{IB} = 60$ cm, so the effective cell aspect ratio was $\mathcal{L} = L/H_{IB} = 2/3$. Here, we modelled the porous medium used in Neufeld *et al.* (2010) by adopting a small anisotropy ratio such that Hele-Shaw equations (and Hele-Shaw cells) recover the Darcian regime. The latter regime is achieved for $\epsilon = 5 \times 10^{-4}$. Notice that a fully analogue anisotropy ratio for the Neufeld *et al.* (2010) experiments should be one order of magnitude smaller. However, for such a tiny value of ϵ , numerical experiments

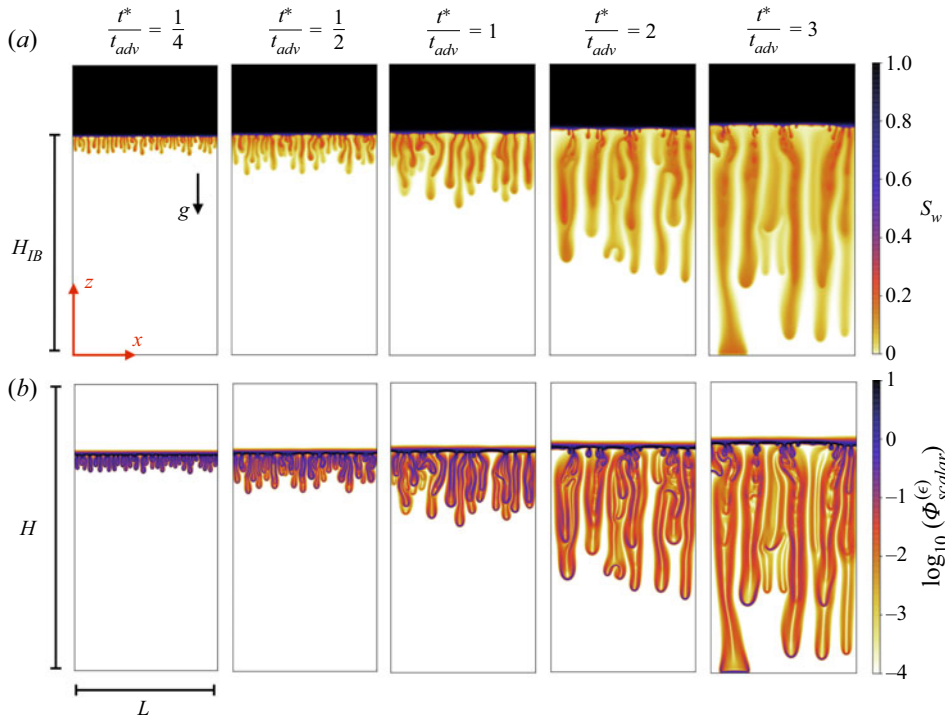


Figure 3. Mass fraction S_w and scalar dissipation rate $\Phi_{scalar}^{(\epsilon)}$ for the mixing of the initial two-fluid system in a Hele-Shaw cell, with $\mathcal{L} = L/H_{IB} = 2/3$, $L/H = 1/2$, $\Delta_w = 0.3$, $Sc = 10$, $Ra = 10^4$ and $\epsilon = 5 \times 10^{-4}$. Slides are shown for different times. The advective time scale is defined as $t_{adv} = H_{IB}/u_c$.

become considerably more expensive while not providing new results. For the adopted value of ϵ , and considering cell height $H = 80$ cm, an experimental Hele-Shaw cell must have cell gap $b = \sqrt{12} \epsilon H \approx 1.5$ mm and fulfil $\epsilon^2 Ra \ll 1$ (Letelier *et al.* 2019; De Paoli *et al.* 2020) – i.e. the Rayleigh number should be no larger than 4×10^5 .

Figure 3 shows the spatiotemporal evolution of the mass fraction S_w and the scalar dissipation rate $\Phi_{scalar}^{(\epsilon)}$ to illustrate the solutal convection and mixing in the two-fluid system. The non-dimensional parameters of the numerical experiment are $\Delta_w = 0.3$, $Sc = 10$ and $Ra = 10^4$. Figure 3(a) encompasses a time window that captures the emergence of instabilities in the early convection or flux growth regime (Slim 2014; Amooie *et al.* 2018) and snapshots illustrating the late convection or constant flux regime, until the first megaplume reaches the bottom boundary. After the onset of convection, lateral diffusion leads to a continuous process of coalescence, where two or more plumes merge, creating megaplumes that enhance downward mass transfer. Simultaneously, figure 3(b) shows the scalar dissipation rate $\Phi_{scalar}^{(\epsilon)}$, highlighting that vigorous mixing occurs at the diffusive layer and edges of convective plumes. The latter demonstrates that horizontal diffusion is an active process in the convective region, as posited by Neufeld *et al.* (2010). Additionally, figure 3 shows the slow yet pervasive interface upward displacement caused in response to the continuous bloom of proto-plumes.

Figure 4 shows time series for the mean dissipation rate of the scalar variance, $\langle \Phi_{scalar}^{(\epsilon)} \rangle_v$, for $\epsilon = 5 \times 10^{-4}$ and $Ra = 3000$, 10 000 and 30 000. During the onset of

Scaling CO₂-brine mixing in permeable media via analogue models

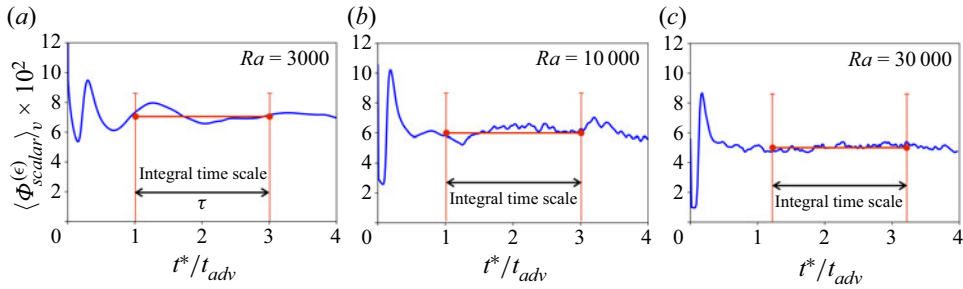


Figure 4. Time series of the mean scalar dissipation rate $\langle \Phi_{scalar}^{(\epsilon)} \rangle_v$ for $\epsilon = 5 \times 10^{-4}$ and $3 \times 10^3 \leq Ra \leq 3 \times 10^4$.

convection due to cabbeling and after the diffusive regime, $\langle \Phi_{scalar}^{(\epsilon)} \rangle_v$ shows a transient behaviour characterised by a sharp and large amplitude peak, associated with the flux growth regime. This first peak is followed by a relaxation phase associated with the merging regime. The mergers between primary plumes continue, but the system reaches a quasi-steady rate of decay of the scalar variance φ^2 within the volume $\Omega_c(t)$, governed by the second conservation equation (3.14) – the late convection regime. This result allows us to define an *ad hoc* integral time scale τ that characterises the period over which $\langle \Phi_{scalar}^{(\epsilon)} \rangle_v$ is statistically steady, until the first megaplume reaches the bottom. Note that at the quasi-steady state, the mean dissipation rate of the scalar variance decreases as the Rayleigh number increases, showing a functional dependence between $\langle \Phi_{scalar}^{(\epsilon)} \rangle_v$ and Ra .

Figure 5 shows time series of the physical quantities governing the first conservation equation (3.9), for two numerical experiments, with $\epsilon = 5 \times 10^{-4}$, and $Ra = 10^4$ and $Ra = 3 \times 10^4$, respectively. Each panel highlights the integral time scale τ . The evolution in time of the averaged height $h(t)$ is shown in figures 5(a,d). The results illustrate that $h(t)$ grows linearly, implying that the convective region B expands vertically at a constant rate. The latter is remarkable since it indicates that global quantities and boundary fluxes, such as $d\langle \varphi \rangle_v / dt$ and $(\partial \langle \varphi \rangle_\ell / \partial z)|_{z=h}$, reach statistically steady states over τ , shown in figures 5(b,e) and 5(c,f), respectively. Hence we can rigorously link the controlling parameters ϵ and Ra with the global Sherwood number Sh_φ .

Figure 6(a) maps the relationship between Sh_φ and Ra , integrating numerical simulations and laboratory experimental data reported by Neufeld *et al.* (2010) plus our numerical results. We computed the mass transfer rate as (3.10), the global Sherwood number. For $\epsilon = 5 \times 10^{-4}$ and the intermediate Ra range, $10^3 \leq Ra \leq 3 \times 10^4$, the numerical results lead to the scaling law $Sh_\varphi = \tilde{b} Ra^{\tilde{n}}$, valid for the Darcian regime, with $\tilde{b} = 0.12 \pm 0.02$ and $\tilde{n} = 0.83 \pm 0.01$. The latter is equivalent to the results by Neufeld *et al.* (2010). Remarkably, figure 6(b) shows that the ratio of the Sherwood number and mean scalar dissipation rate, ϑ_{scalar} , scales as $Sh_\varphi / \vartheta_{scalar} = b Ra^n$, with $b = 5.4 \pm 0.4$ and $n = 0.99 \pm 0.01$. This result is analogous to the scaling law $Nu = Ra \vartheta_{scalar}$, with Nu the Nusselt number, which governs irreversible thermal mixing and heat transfer in Rayleigh–Bénard–Darcy convection (Letelier *et al.* 2019; Ulloa & Letelier 2022). Therefore, results in figure 6(b) indicate that ϑ_{scalar} depends on Ra in the range of intermediate Ra , and for adiabatic analogue models in the Darcian regime, $Sh_\varphi \sim Ra \vartheta_{scalar}$. Experimental results reported by Neufeld *et al.* (2010) support the existence of a persistent sub-linear relation $Sh_\varphi \sim Ra^\alpha$ up to $Ra \lesssim 10^5$.

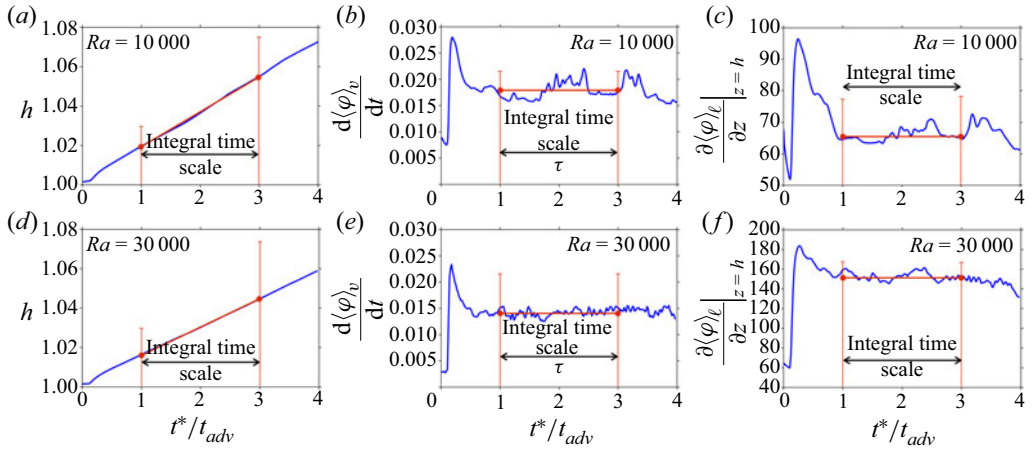


Figure 5. Time series of two numerical experiments, for $\epsilon = 5 \times 10^{-4}$, $Ra = 10^4$ and $Ra = 3 \times 10^4$. (a,d) Height h characterising the isoscalar surface $S_w = 2\Delta_w$ as a function of time. Here, h has a fairly constant rate of change in time, $dh/dt = w_{int}$. (b,e) Rate of change in time of mean scalar $\langle\varphi\rangle_v$. (c,f) Time series of the vertical gradient of the laterally averaged scalar $\langle\varphi\rangle_\ell$ at $z = h$.

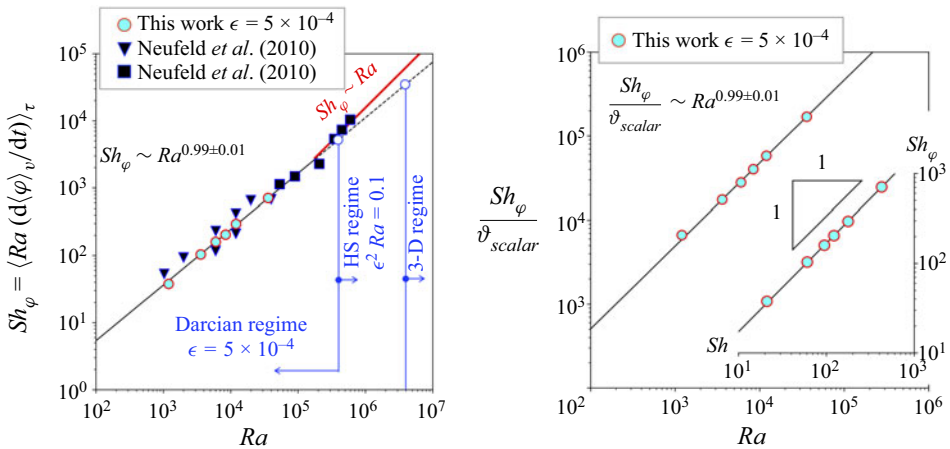


Figure 6. Scaling laws for the mass transfer rate across the average height $h(t)$ between the miscible fluids mimicking the CO_2 -brine mixture. (a) Plots of Sh_φ versus Ra in the Darcian regime, i.e. $\epsilon^2 Ra \leq 0.1$ (where HS stands for Hele-Shaw). Black triangles and black squares were obtained from numerical and laboratory experiments, respectively, reported by Neufeld *et al.* (2010). For $\epsilon = 5 \times 10^{-4}$, our numerical experiments shown in cyan circles lead to a scaling law $Sh_\varphi \sim Ra^{0.83 \pm 0.01}$ valid for $Ra \lesssim 10^5$. (b) The main panel shows $Sh_\varphi / \vartheta_{scalar}$ versus Ra for the numerical experiments. Results lead to the scaling law $Sh_\varphi / \vartheta_{scalar} \sim Ra^{0.99 \pm 0.01}$. Inset shows the global Sherwood number Sh_φ versus the local Sherwood number Sh , obtaining the relationship $Sh \sim Sh_\varphi$.

For $Ra \gtrsim 10^5$ (high- Ra), experimental data seem to fit the linear relation $Sh_\varphi \sim Ra$. Regarding the solutal Nusselt number Nu_φ , we obtain the sub-linear relations $Nu_\varphi \sim Ra^{0.78}$ and $Nu_\varphi / \vartheta_{scalar} \sim Ra^{0.94}$ in the range of intermediate Ra . Regardless of the metric used to estimate the mass flux (Sh_φ or Nu_φ), $\vartheta_{scalar} \sim Ra^{-0.16}$.

It is relevant to mention that experiments in 3-D porous environments lead to mass fluxes about 25% higher than those estimated for 2-D porous media, but the scaling

tendency is quite similar. This increase in the mass flux for 3-D over 2-D laboratory results is consistent with the numerical simulations by Amooie *et al.* (2018) and with the increase in heat transfer of about 18% obtained for 3-D over 2-D thermal convection by Pirozzoli *et al.* (2021), both numerical studies being grounded on Darcy models.

In the context of CO₂ dissolution trapping into deep aquifers, our findings show that the mass transfer of CO₂ gas phase into aqueous brine should be proportional to the decay rate of dissolved CO₂ variance in the aqueous phase. This suggests that the irreversible mixing rate occurring in the convective region Ω_c is an essential process governing the CO₂ geologic sequestration. Indeed, the non-dimensional, time-averaged mass flux \mathcal{F} scales as $Sh_\varphi/Ra \sim \vartheta_{scalar}$.

5.2. Revisiting the scaling laws for mass transfer in porous media

Amooie *et al.* (2018) suggest that lateral boundaries do not significantly affect the scaling laws between the Sherwood number and Rayleigh number as long as the full development of megaplumes is free from the extent of the horizontal domain. However, experimental realisations inherently have limited cell aspect ratios, regardless of whether they employ porous media or Hele-Shaw cells in the Darcian regime. This experimental constraint leads to sub-linear relationships $Sh_\varphi \sim Ra^\alpha$, i.e. $0 \leq \alpha < 1$, as shown in § 5.1. Here, we examine how the finite extent of the horizontal domain could modify the value of the exponent α . To mimic large cell aspect ratios, we utilise the Hele-Shaw equations in the Darcian regime applied for the analogue model with periodic lateral boundary conditions.

Adopting the same parameters for the Hele-Shaw cell described in § 5.1, figure 7 illustrates the relationship between Sh_φ and Ra obtained from our numerical simulations with periodic lateral boundaries. The results show a sub-linear scaling law $Sh_\varphi = \tilde{b} Ra^{\tilde{n}}$, with $\tilde{b} = 0.07 \pm 0.02$ and $\tilde{n} = 0.88 \pm 0.03$, valid for the intermediate range $10^3 \lesssim Ra \lesssim 3 \times 10^4$, which differs from $Sh_\varphi \sim Ra^{0.83 \pm 0.01}$ obtained for closed boundaries. Moreover, the inset in figure 7 shows that $Sh_\varphi/\vartheta_{scalar} = b Ra^n$, with $b = 5.4 \pm 0.5$ and $n = 0.99 \pm 0.01$. Therefore, the relation $Sh \sim Ra \vartheta_{scalar}$ is also attained for periodic boundary conditions. These results suggest a redistribution of mass within the (periodic or large) convective domain $\Omega_c(t)$ that enhances the global mass transfer. Here, the remarkable result is the ‘universality’ of the scaling law $Sh_\varphi \sim Ra \vartheta_{scalar}$, regardless of the lateral boundary condition employed in the analogue model. Therefore, for intermediate Ra , the relations $Sh_\varphi \sim Ra^\alpha$ and $\vartheta_{scalar} \sim Ra^{\alpha-1}$ are sensitive to (i) the adopted model (canonical or analogue), (ii) the lateral boundary conditions, and (iii) the range of Ra considered.

The approximate relation $Sh_\varphi \sim Ra^{0.9}$ obtained in this section, valid for the range $10^3 \lesssim Ra \lesssim 3 \times 10^4$, agrees with the scaling law $Sh \sim Ra^{0.9}$ suggested by Amooie *et al.* (2018) for the constant-composition condition applied in the canonical model. Interestingly, our result also agrees with the scaling $Nu \sim Ra^{0.9}$ obtained numerically for ‘wall to wall’ heat transfer in porous media (Hewitt *et al.* 2012) and Hele-Shaw domains in the Darcian regime (Letelier *et al.* 2019). For high Ra values ($Ra \gtrsim 4 \times 10^4$) and periodic lateral boundaries, we remark that both problems, heat and mass transport, seem to satisfy, asymptotically, the linear scaling laws $Nu \sim Ra$ and $Sh_\varphi \sim Ra$, respectively. A consequence of the above is that ϑ_{scalar} is insensitive to Ra , recovering the findings reported by Hidalgo *et al.* (2012) for the analogue model with periodic lateral boundaries.

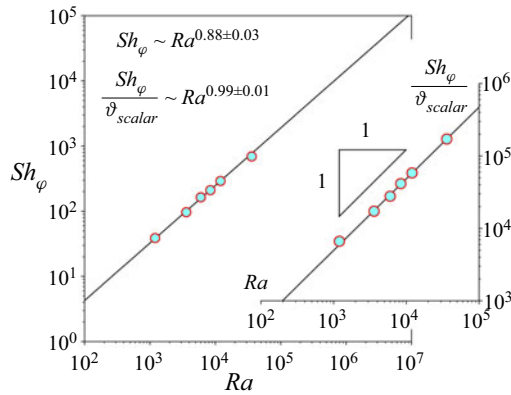


Figure 7. Numerical results for the analogue problem with periodic boundary conditions (Hidalgo *et al.* 2012). The main plot illustrates Sh_φ versus Ra , showing that the global Sherwood number and Rayleigh number satisfy the scaling law $Sh_\varphi \sim Ra^{0.88 \pm 0.03}$. Inset illustrates $Sh_\varphi / \vartheta_{scalar}$ versus the Rayleigh number Ra , obtaining the relationship $Sh_\varphi / \vartheta_{scalar} \sim Ra^{0.99 \pm 0.01}$.

5.3. The adiabatic Hele-Shaw model predictions

Figure 8(a) maps the relationship between Ra and Sh_φ , including an additional set of numerical experiments for $\epsilon = 5 \times 10^{-3}$, to explore the system’s response beyond the Darcian regime. For $\epsilon = 5 \times 10^{-3}$, we observe that for $Ra \leq 4000$, the dataset follows the power law given by the Darcian regime, $Sh_\varphi \sim Ra^{0.83 \pm 0.01}$. However, for $\epsilon^2 Ra \geq 0.1$, 3-D effects start to influence the global mixing rate, diminishing the mass transfer across the interface in a fashion similar to that observed in Rayleigh–Bénard–Darcy convection (Letelier *et al.* 2019). Such a dependence between the convective flow dimensionality and the power-law exponent may explain the experimental scaling law $Sh \sim Ra^{0.76}$ obtained by Backhaus *et al.* (2011) in Hele-Shaw cells. Their exponent, 0.76, strongly suggests the transition from Darcian to Hele-Shaw regime.

One might want to integrate the Hele-Shaw model results with laboratory experiments. However, linking recent Hele-Shaw experiments with our numerical results is challenging because experimental data are grouped in terms of cell gap b rather than ϵ . We overcome this issue by utilising an alternative pair of non-dimensional parameters: the Péclet number, defined as

$$Pe = \epsilon Ra = \frac{u_c \sqrt{K}}{\kappa}, \tag{5.1}$$

and the modified Sherwood number, defined as

$$Sh_\varphi^{(m)} = \left\langle Pe \frac{d\langle \varphi \rangle_v}{dt} \right\rangle_\tau. \tag{5.2}$$

Figure 8(b) merges our numerical experiments and the recent laboratory studies in Hele-Shaw cells by De Paoli *et al.* (2020) (canonical model) and Ecke & Backhaus (2016) (analogue model). In both laboratory studies, the mass flux exhibits an almost constant magnitude for a fixed cell gap. Each square and triangle in figure 8(b) represents the mean value of five experiments with the same b , respectively. For numerical experiments with $\epsilon = 5 \times 10^{-3}$, a bifurcation from Darcian to Hele-Shaw regime is observed for Rayleigh numbers larger than 4000. In the Hele-Shaw regime, inertial effects become more

Scaling CO_2 -brine mixing in permeable media via analogue models

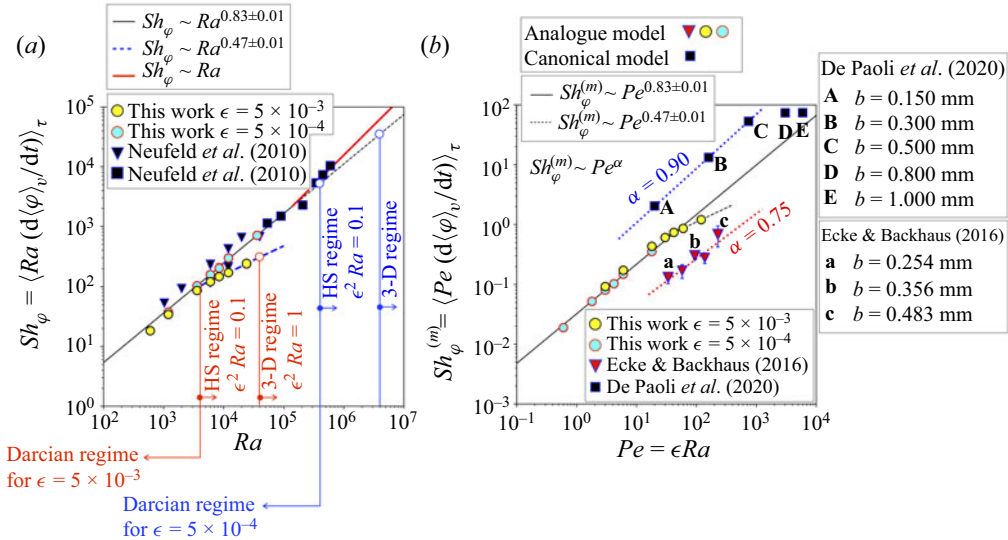


Figure 8. Scaling laws for the mass transfer rate across the average height $h(t)$ between the miscible fluids for Darcian, Hele-Shaw (HS), and 3-D regimes. Each regime is $\epsilon^2 Ra$ -dependent. For $\epsilon = 5 \times 10^{-3}$ (yellow circles), the Darcian regime is upper bounded by $Ra \approx 4 \times 10^3$, whereas the HS regime is associated with $4 \times 10^3 \lesssim Ra \lesssim 4 \times 10^4$. (a) Plots of Sh_φ versus Ra . Black triangles and black squares were obtained from numerical and laboratory experiments, respectively, reported by Neufeld et al. (2010). Our numerical experiments in the HS regime (yellow circles) show a scaling law $Sh_\varphi \sim Ra^{0.47 \pm 0.01}$. (b) Modified Sherwood number $Sh_\varphi^{(m)}$ versus Péclet number $Pe = \epsilon Ra$, for laboratory experiments in Hele-Shaw cells (Ecke & Backhaus 2016; De Paoli et al. 2020) and our numerical experiments. De Paoli et al. (2020) utilised the canonical model in their experimental configuration, while Ecke & Backhaus (2016) used the analogue model. The values of the exponent α for each dataset show its dependence on the (canonical or analogue) model used and the effects of the cell gap on mass transfer.

vigorous, leading to a scaling law with a lower exponent, $Sh_\varphi^{(m)} \sim Pe^{0.47 \pm 0.01}$. Physically, this means that widening the cell aperture results in a global enhancement of the scalar homogenisation and the reduction of scalar gradients due to the volume expansion across the cell gap. We stress the behaviour of points D and E from the dataset of De Paoli et al. (2020), which depart from the power-law prediction valid for the Darcian regime in the canonical model. The latter is due to the full 3-D effects supported by Hele-Shaw cells with wide apertures and high Ra (Letelier et al. 2019; De Paoli et al. 2020).

In summary, laboratory and numerical experiments prove that the power law between Sh_φ and Ra is ϵ -dependent. Nonetheless, we show that the functional relationship between the ratio $Sh_\varphi / \vartheta_{scalar}$ and the Rayleigh number collapses all the numerical experiments, revealing the existence of a universal scaling law – independent of ϵ and directly proportional to Ra . Figure 9 crystallises the relationship $Sh_\varphi / \vartheta_{scalar} \sim Ra$. This result is significant since it links three fundamental quantities: the Sherwood number Sh , the Rayleigh number Ra , and the mean scalar dissipation rate ϑ_{scalar} .

5.4. Implications for CO_2 -brine mixing at the field scale

Deep brine aquifers are the most promising geologic reservoirs to store CO_2 underground permanently due to their large storage capacity (Rathnaweera & Ranjith 2020). However, the low solubility of injected supercritical CO_2 into brines, about 3–5 %

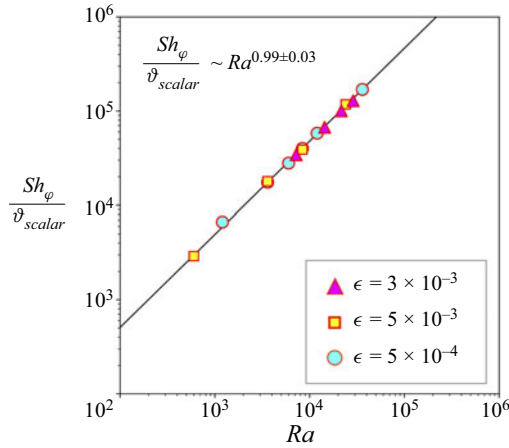


Figure 9. Scaling law for $Sh_\varphi/\vartheta_{scalar}$ with Ra for three set of numerical experiments with $Sc = 10$ and different ϵ . All experiments collapse to the curve $Sh_\varphi/\vartheta_{scalar} \sim Ra^{0.99\pm 0.01}$.

(Mohammadian *et al.* 2015), is a significant drawback that makes CO₂ sequestration inefficient on short time scales, limiting its feasibility. Furthermore, due to its low solubility and positive buoyancy relative to the surrounding natural porous fluids, the (significant) part of CO₂ gas phase, not dissolved in brine, might potentially leak through fractures in the caprock and reach the atmosphere to become a source.

To increase the mixing and dissolution, studies have shown that adding high-mass, ultra-small size nanoparticles (NPs) into the injected CO₂ can (i) accelerate the onset time of convection, (ii) enhance the mixing of dissolved CO₂ with the underlying brine, and (iii) reduce the risk of leakage (e.g. Javadpour & Nicot 2011). Doping CO₂ with NPs allows increasing the density contrast between the CO₂-NPs-brine mixture and the underlying brine. The latter strengthens convection, increasing the velocity scale u_c of megaplumes, and consequently amplifying Ra and Sh_φ . Typically, in idealised reservoirs, $Ra \sim 10^4$ (Neufeld *et al.* 2010). Let us consider a large lateral spread of mobile CO₂ gas phase within a reservoir. In this scenario, we can estimate changes in the Sherwood number utilising the sub-linear scaling $Sh_\varphi \sim Ra^{0.9}$ (proposed in § 5.2) as a first approximation. The latter implies that ϑ_{scalar} depends on Ra .

A relevant open question is as follows. (i) How much can the density contrast be increased to enhance the mass transfer between the CO₂-rich brine and the underlying brine? Here, the mean scalar dissipation rate begins to play a fundamental role. For the canonical model, Amooie *et al.* (2018) demonstrate the linear scaling law $Sh_\varphi \sim Ra$, valid for $Ra \gtrsim 4 \times 10^4$. In this linear regime, ϑ_{scalar} is invariant to Ra . For the CO₂-brine mixture at the field scale, ϑ_{scalar} may have a ‘saturation condition’, regardless of the increase of Sh_φ due to the addition of high-mass NPs. In other words, this condition supports the existence of a ‘constant mixing rate phase’ in which the dissolved CO₂ homogenises in the bulk of the deep aquifer at a constant rate via irreversible mixing. An estimation of the ‘transition’ Ra , Ra_T , that would lead to the ‘constant mixing rate phase’ must be investigated. Reaching this phase is intriguing since increasing Ra above Ra_T powers an increment in the available energy that strengthens convection (kinetic energy) and enhances mass flux yet at a constant ϑ_{scalar} . The latter leads to addition fundamental questions. (ii) How is the energy excess in the two-fluid system expended? (iii) Does

the kinetic energy dissipation rate also saturate above Ra_T ? These questions warrant further research on the production and dissipation processes associated with CO₂-rich brine convection.

6. Concluding remarks

Geologic carbon sequestration in brine aquifers is a geoengineering method proposed to decarbonise the Earth's atmosphere, mitigating climate change and its impacts. The latter is a response to the call of Sustainable Development Goal 13: Climate Action, defined in the 2030 Agenda by the United Nations. Yet strategies to improve the efficiency of underground CO₂ sequestration remain debated, requiring a deeper understanding of long-term capture processes. In particular, the influence of the mean (CO₂) scalar dissipation rate in the dissolution dynamics within terrestrial reservoirs has been given little attention. Here, we investigated the fluid dynamics and irreversible mixing for a two-fluid system in permeable media, mimicking processes catalysing the CO₂ dissolution trapping in deep brine aquifers. For the above, we utilised the Hele-Shaw equations (Letelier *et al.* 2019) and analogue, laboratory-inspired models with a nonlinear equation of state for density.

The fluid dynamics and mixing of the two-fluid system is powered by a cabling process that fosters a continuous growth of protoplumes from the diffusive boundary layer. These protoplumes become convective plumes, which in turn form megaplumes due to coalescence. Irreversible mixing occurs due to diapycnal mass flux, i.e. a flux in the direction normal to the local isopycnal surface. This irreversible flux is proportional to the rate at which the scalar spatial variance decays in time, $\Phi_{scalar}^{(\epsilon)}$.

The convective region beneath the 'interface' contributes significantly to the irreversible global mixing. In the convective region, our numerical results show that mixing occurs intensively at the edges of the megaplumes and mostly across the lateral \hat{x} direction, as proposed by Neufeld *et al.* (2010). Consistently with the Q-2-D porous medium laboratory experiments performed by Neufeld *et al.* (2010), our numerical experiments in the Darcian regime ($\epsilon^2 Ra \ll 1$) show a sub-linear scaling $Sh_\varphi \sim Ra^\alpha$, with $\alpha = 0.83 \pm 0.01$.

From our results, we see that Hele-Shaw experiments must account carefully for the dynamic regimes controlled by the Péclet number and the anisotropy ratio. Employing the Hele-Shaw model (Letelier *et al.* 2019), we were able to achieve the Darcian regime for $\epsilon Pe \leq 0.1$. The latter allows modelling and studying the CO₂ sequestration in porous media (Neufeld *et al.* 2010; Guo *et al.* 2021). To reconcile laboratory experiments in porous media and Hele-Shaw cells, we illustrated results in the Hele-Shaw regime (Letelier *et al.* 2019; De Paoli *et al.* 2020), in which inertial effects become measurable and the Darcian regime breaks down. We expect Hele-Shaw experiments that do not comply with the Darcian regime to lead to scaling laws with exponents lower than $\alpha \approx 0.83$. This reduction in the power-law exponent is associated with an enhancement of the scalar field homogenisation, as shown via laboratory experiments by De Paoli *et al.* (2020) and more recently by Noto, Ulloa & Letelier (2022, 2023). Therefore, weak inertial effects in the Hele-Shaw regime might explain the sub-linear power law $Sh \sim Ra^{0.76}$ reported by Backhaus *et al.* (2011).

Finally, it is remarkable that buoyancy-driven convective flows in vertical Hele-Shaw geometries under quasi-steady state admit a universal law given by $\mathcal{F}_\varphi = b_\varphi Ra \vartheta_{scalar}$, with \mathcal{F}_φ the scalar transport related to φ – i.e. heat (Nu) or mass transfer (Sh_φ) – and ϑ_{scalar} , the mean dissipation rate of φ . The parameter b_φ takes the value $b_\varphi = 1$ for heat transfer, but for mass transfer in analogue models, $b_\varphi \sim 5.4$ when $\Delta_w = 0.3$. Exploring the

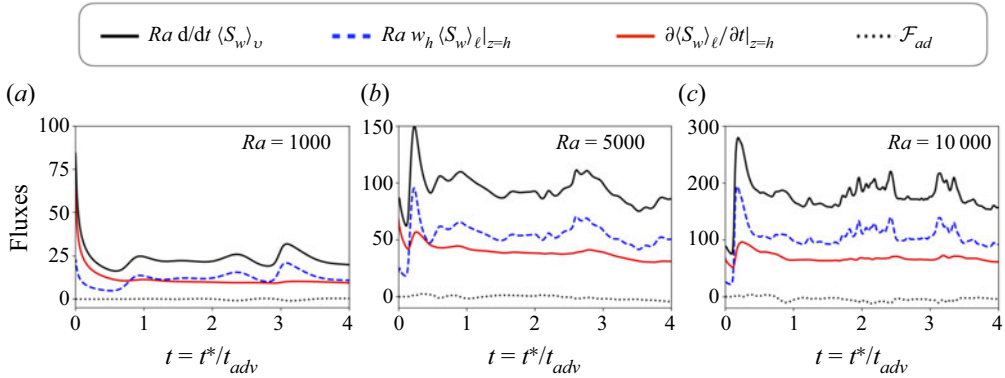


Figure 10. Time series of various non-dimensional fluxes involved in time evolution of the mean scalar field $\langle S_w \rangle_v$ for three Rayleigh numbers, $10^3 \leq Ra \leq 10^4$. The solid line denotes the rate of change in time of the mean scalar field in the domain Ω_c ; the dashed line denotes the advective flux at the upper mobile boundary at $z = h(t)$; the red solid line denotes the diffusive flux; and the dotted line denotes the advection–dispersion flux at the mobile boundary $z = h(t)$.

implications of this universal law at field scale warrants further research to investigate mechanisms capable of enhancing CO₂ dissolution and storage in deep brine aquifers.

Acknowledgements. This research was partially supported by the supercomputing infrastructure of the National Laboratory High Performance Computing NLHPC (ECM-02). H.N.U. acknowledges support from SAS GPC at University of Pennsylvania. We thank D. Noto and X. Trujillo for critical reading and comments. Finally, we are grateful for the remarkable feedback provided by three anonymous reviewers.

Funding. J.L. acknowledges the support from ANID Fellowship no. 21191043. J.H.O. acknowledges support from Centro de Modelamiento Matemático (CMM) grant ANID ACE210010 and Basal FB210005, and also Fondecyt grant 1201125.

Declaration of interests. The authors report no conflict of interest.

Author ORCIDs.

📍 J.A. Letelier <https://orcid.org/0000-0002-4679-1210>;

📍 H.N. Ulloa <https://orcid.org/0000-0002-1995-6630>.

Appendix. Time series of the first conservation law (3.7)

Figure 10 illustrates time series of the fluxes governing the evolution of the mean scalar field S_w representing the dissolved CO₂ in brine within the time-varying volume $\Omega_c(t)$. This volume characterises the region where cabbeling-powered convection takes place. Figure 10 summarises results for three Rayleigh numbers, $Ra = 10^3$ in figure 10(a), $Ra = 5 \times 10^3$ in figure 10(b), and $Ra = 10^4$ in figure 10(c). The rate of change in time of $\langle S_w \rangle_v$ is shown in the black solid line. The blue dashed line denotes the advective flux $Ra w_h \langle S_w \rangle_\ell|_{z=h}$. The red solid line is diffusive flux at the upper mobile boundary $z = h(t)$ of $\Omega_c(t)$, i.e. $\partial \langle S_w \rangle_\ell / \partial z|_{z=h}$. The dotted line represents the advective–dispersive flux at $z = h(t)$, i.e. \mathcal{F}_{ad} . The numerical experiments show that \mathcal{F}_{ad} has a minor contribution in the overall evolution of $\langle S_w \rangle_v$. In contrast, the most prominent flux is the advection at the mobile upper boundary. Indeed, $Ra w_h \langle S_w \rangle_\ell|_{z=h}$ modulates the time series of $Ra d \langle S_w \rangle_v / dt$. This dominance is especially evident at high Ra (figure 10c), whereas at low Ra , advection and diffusive fluxes have similar contributions.

REFERENCES

- ALIPOUR, M., DE PAOLI, M. & SOLDATI, A. 2020 Concentration-based velocity reconstruction in convective Hele-Shaw flows. *Exp. Fluids* **61** (9), 195.
- ALTMAN, S.J., *et al.* 2014 Chemical and hydrodynamic mechanisms for long-term geological carbon storage. *J. Phys. Chem. C* **118** (28), 15103–15113.
- AMOOIE, M.A., SOLTANIAN, M.R. & MOORTGAT, J. 2018 Solutal convection in porous media: comparison between boundary conditions of constant concentration and constant flux. *Phys. Rev. E* **98** (3), 033118.
- ARIAS, P.A., *et al.* 2021 Technical summary. In *Climate Change 2021: The Physical Basis. Contribution of Working Group I to the Sixth Assessment Report of the Intergovernmental Panel on Climate Change* (ed. V. Masson-Delmotte, *et al.*). Cambridge University Press. 33–144.
- BACKHAUS, S., TURITSYN, K. & ECKE, R.E. 2011 Convective instability and mass transport of diffusion layers in a Hele-Shaw geometry. *Phys. Rev. Lett.* **106** (10), 104501.
- CELIA, M.A., BACHU, S., NORDBOTTEN, J.M. & BANDILLA, K.W. 2015 Status of CO₂ storage in deep saline aquifers with emphasis on modeling approaches and practical simulations. *Water Resour. Res.* **51** (9), 6846–6892.
- DE PAOLI, M. 2021 Influence of reservoir properties on the dynamics of a migrating current of carbon dioxide. *Phys. Fluids* **33** (1), 016602.
- DE PAOLI, M., ALIPOUR, M. & SOLDATI, A. 2020 How non-Darcy effects influence scaling laws in Hele-Shaw convection experiments. *J. Fluid Mech.* **892**, A41.
- DE PAOLI, M., PERISSUTTI, D., MARCHIOLI, C. & SOLDATI, A. 2022 Experimental assessment of mixing layer scaling laws in Rayleigh–Taylor instability. *Phys. Rev. Fluids* **7** (9), 093503.
- ECKE, R.E. & BACKHAUS, S. 2016 Plume dynamics in Hele-Shaw porous media convection. *Phil. Trans. R. Soc. Lond. A* **374** (20150420), 20150420.
- FRIEDMANN, S.J. 2007 Geological carbon dioxide sequestration. *Elements* **3** (3), 179–184.
- GROESKAMP, S., ABERNATHEY, R.P. & KLOCKER, A. 2016 Water mass transformation by cabbelling and thermobaricity. *Geophys. Res. Lett.* **43** (20), 10835–10845.
- GRÖTZBACH, G. 1983 Spatial resolution requirements for direct numerical simulation of the Rayleigh–Bénard convection. *J. Comput. Phys.* **49** (2), 241–264.
- GUO, R., SUN, H., ZHAO, Q., LI, Z., LIU, Y. & CHEN, C. 2021 A novel experimental study on density-driven instability and convective dissolution in porous media. *Geophys. Res. Lett.* **48** (23), e2021GL095619.
- HEWITT, D.R., NEUFELD, J.A. & LISTER, J.R. 2012 Ultimate regime of high Rayleigh number convection in a porous medium. *Phys. Rev. Lett.* **108** (22), 224503.
- HEWITT, D.R., NEUFELD, J.A. & LISTER, J.R. 2013 Convective shutdown in a porous medium at high Rayleigh number. *J. Fluid Mech.* **719**, 551–586.
- HIDALGO, J.J., DENTZ, M., CABEZA, Y. & CARRERA, J. 2015 Dissolution patterns and mixing dynamics in unstable reactive flow. *Geophys. Res. Lett.* **42** (15), 6357–6364.
- HIDALGO, J.J., FE, J., CUETO-FELGUEROSO, L. & JUANES, R. 2012 Scaling of convective mixing in porous media. *Phys. Rev. Lett.* **109** (26), 264503.
- HUPPERT, H.E. & NEUFELD, J.A. 2014 The fluid mechanics of carbon dioxide sequestration. *Annu. Rev. Fluid Mech.* **46** (1), 255–272.
- JAVADPOUR, F. & NICOT, J.-P. 2011 Enhanced CO₂ storage and sequestration in deep saline aquifers by nanoparticles: commingled disposal of depleted uranium and CO₂. *Transp. Porous Med.* **89** (2), 265–284.
- KHATTAB, I.S., BANDARKAR, F., KHOUBNASABJAFARI, M. & JOUYBAN, A. 2017 Density, viscosity, surface tension, and molar volume of propylene glycol + water mixtures from 293 to 323 K and correlations by the Jouyban–Acree model. *Arab. J. Chem.* **10**, S71–S75.
- LETÉLIER, J.A., HERRERA, P., MUJICA, N. & ORTEGA, J.H. 2016 Enhancement of synthetic schlieren image resolution using total variation optical flow: application to thermal experiments in a Hele-Shaw cell. *Exp. Fluids* **57** (2), 18.
- LETÉLIER, J.A., MUJICA, N. & ORTEGA, J.H. 2019 Perturbative corrections for the scaling of heat transport in a Hele-Shaw geometry and its application to geological vertical fractures. *J. Fluid Mech.* **864**, 746–767.
- LIANG, Y., WEN, B., HESSE, M.A. & DICARLO, D. 2018 Effect of dispersion on solutal convection in porous media. *Geophys. Res. Lett.* **45** (18), 9690–9698.
- MACMINN, C.W. & JUANES, R. 2013 Buoyant currents arrested by convective dissolution. *Geophys. Res. Lett.* **40** (10), 2017–2022.
- METZ, B., DAVIDSON, O., DE CONINCK, H.C., LOOS, M. & MEYER, L.A. (Eds) 2005 *IPCC Special Report on Carbon Dioxide Capture and Storage. Prepared by Working Group III of the Intergovernmental Panel on Climate Change*. Cambridge University Press.

- MOHAMMADIAN, E., HAMIDI, H., ASADULLAH, M., AZDARPOUR, A., MOTAMEDI, S. & JUNIN, R. 2015 Measurement of CO₂ solubility in NaCl brine solutions at different temperatures and pressures using the potentiometric titration method. *J. Chem. Engng Data* **60** (7), 2042–2049.
- NEUFELD, J.A., HESSE, M.A., RIAZ, A., HALLWORTH, M.A., TCHELEPI, H.A. & HUPPERT, H.E. 2010 Convective dissolution of carbon dioxide in saline aquifers. *Geophys. Res. Lett.* **37** (22), L22404.
- NOTO, D., ULLOA, H.N. & LETELIER, J.A. 2022 Energy partitioning of thermally driven flows confined in Hele-Shaw systems. In *75th Annual Meeting of the Division of Fluid Dynamics* (ed. L. Castillo & A. Ardekani). Bulletin of the American Physical Society.
- NOTO, D., ULLOA, H.N. & LETELIER, J.A. 2023 Reconstructing temperature fields for thermally-driven flows under quasi-steady state. *Exp. Fluids* **64**, 74.
- PAU, G.S.H., BELL, J.B., PRUESS, K., ALMGREN, A.S., LIJEWSKI, M.J. & ZHANG, K. 2010 High-resolution simulation and characterization of density-driven flow in CO₂ storage in saline aquifers. *Adv. Water Resour.* **33** (4), 443–455.
- PIROZZOLI, S., DE PAOLI, M., ZONTA, F. & SOLDATI, A. 2021 Towards the ultimate regime in Rayleigh–Darcy convection. *J. Fluid Mech.* **911**, R4.
- RATHNAWEERA, T.D. & RANJITH, P.G. 2020 Nano-modified CO₂ for enhanced deep saline CO₂ sequestration: a review and perspective study. *Earth Sci. Rev.* **200**, 103035.
- SLIM, A.C. 2014 Solutal-convection regimes in a two-dimensional porous medium. *J. Fluid Mech.* **741**, 461–491.
- SLIM, A.C., BANDI, M.M., MILLER, J.C. & MAHADEVAN, L. 2013 Dissolution-driven convection in a Hele-Shaw cell. *Phys. Fluids* **25** (2), 024101.
- SUN, T. & TEJA, A.S. 2004 Density, viscosity, and thermal conductivity of aqueous ethylene, diethylene, and triethylene glycol mixtures between 290 K and 450 K. *J. Chem. Engng Data* **49** (5), 1311–1317.
- ULLOA, H.N. & LETELIER, J.A. 2022 Energetics and mixing of thermally driven flows in Hele-Shaw cells. *J. Fluid Mech.* **930**, A16.
- WANG, L., NAKANISHI, Y., HYODO, A. & SUEKANE, T. 2016 Three-dimensional structure of natural convection in a porous medium: effect of dispersion on finger structure. *Intl J. Greenh. Gas Control* **53**, 274–283.
- WINTERS, K.B. & DE LA FUENTE, A. 2012 Modelling rotating stratified flows at laboratory-scale using spectrally-based DNS. *Ocean Model.* **49–50**, 47–59.